Supporting Information for:

Chalcohalide Antiperovskite Thin Films with Visible Light Absorption and High Charge-Carrier Mobility Processed by Solvent-Free and Low-Temperature Methods

Paz Sebastiá-Luna,[a] Nathan Rodkey,[a,b] Adeem Saeed Mirza,[b] Sigurd Mertens,[c] Snigdha Lal,[d] Axel Melchor Gaona Carranza,[a] Joaquín Calbo,[a] Marcello Righetto,[d] Michele Sessolo,[a] Laura M. Herz,[d,e] Koen Vandewal,[c] Enrique Ortí,[a] Mónica Morales-Masis,[b] Henk J. Bolink,[a] and Francisco Palazon[a,f]**

[a] Instituto de Ciencia Molecular, Universidad de Valencia, 46980 Paterna, Spain

[b] MESA+ Institute for Nanotechnology, University of Twente, Enschede 7500 AE, The Netherlands

[c] Institute for Materials Research (IMO-IMOMEC), Hasselt University, Diepenbeek BE – 3590, Belgium

[d] Department of Physics, University of Oxford, Clarendon Laboratory, Parks Road, Oxford OX1 3PU, UK.

[e] Institute for Advanced Study, Technical University of Munich, Lichtenbergstrasse 2a, D-85748 Garching, Germany.

[f] Departamento de Ingeniería Química y Ambiental, Universidad Politécnica de Cartagena, 30202 Cartagena, Spain

Supplementary Note 1: Derivation of charge carrier mobility

The measured fractional THz transmission (ΔT/T) can be converted to the photoconductivity (Δσ) under a thin-film assumption using the equation:[10]

$$\Delta\sigma = -\left[\frac{\epsilon_0 c(n_A + n_B)}{L}\right]\frac{\Delta T}{T}$$

where T is the transmitted THz field strength and ΔT is the photoinduced change in the THz field strength. $n_A = 1$ is the refractive index of vacuum, $n_B = 2.13$ is the refractive index of the quartz substrate and L is the thickness of the sample. ϵ_0 and c are the permittivity of free space and the speed of light respectively.

In order to derive the charge carrier mobility, Δσ can be further defined as:

$$\Delta\sigma = e[\mu_h p + \mu_e n]$$

where e is the electronic charge, μ_e (μ_h) is the electron (hole) mobility and n (p) is the excess electron (hole) density. Immediately after photoexcitation, the electron and hole density can be equated to the absorbed photon density assuming that each absorbed photon leads to the formation of a single electron-hole pair. Thus, we get:

$$n = p = \frac{N}{A_{eff}L}$$

where N is the total number of absorbed photons and A_{eff} is the effective area of overlap between the pump and THz beam.[11] To obtain the total absorbed photons per pulse, we use:

$$N = \frac{E\lambda}{hc}(1 - R_{pump})(1 - T_{pump})$$

Here, E is the pulse energy, λ is the pump excitation wavelength, R_{pump} and T_{pump} are the fractional reflection and fractional transmission at normal incidence of excitation beam respectively. Combining the equations, we get:

$$\Sigma\mu = -\epsilon_0 c(n_A + n_B)\left[\frac{A_{eff}hc}{eE\lambda(1 - R_{pump})(1 - T_{pump})}\right]\frac{\Delta T}{T}$$

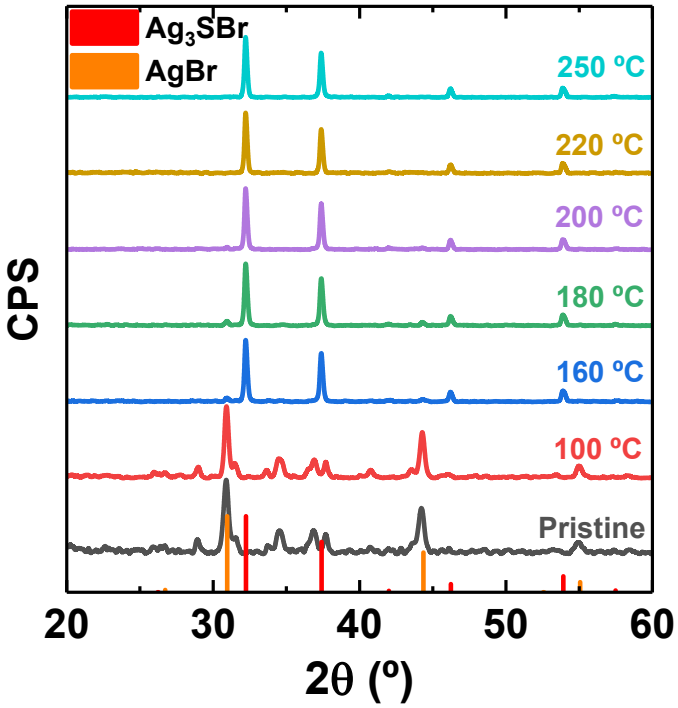

Figure S1. XRD of stoichiometric AgBr+Ag_2S ball-milled for 1 h and annealed at different temperatures for 30 minutes. Reference patterns for Ag_3SBr and AgBr correspond to Inorganic Crystal Structure Database (ICSD) entries #25531 and #56546, respectively.

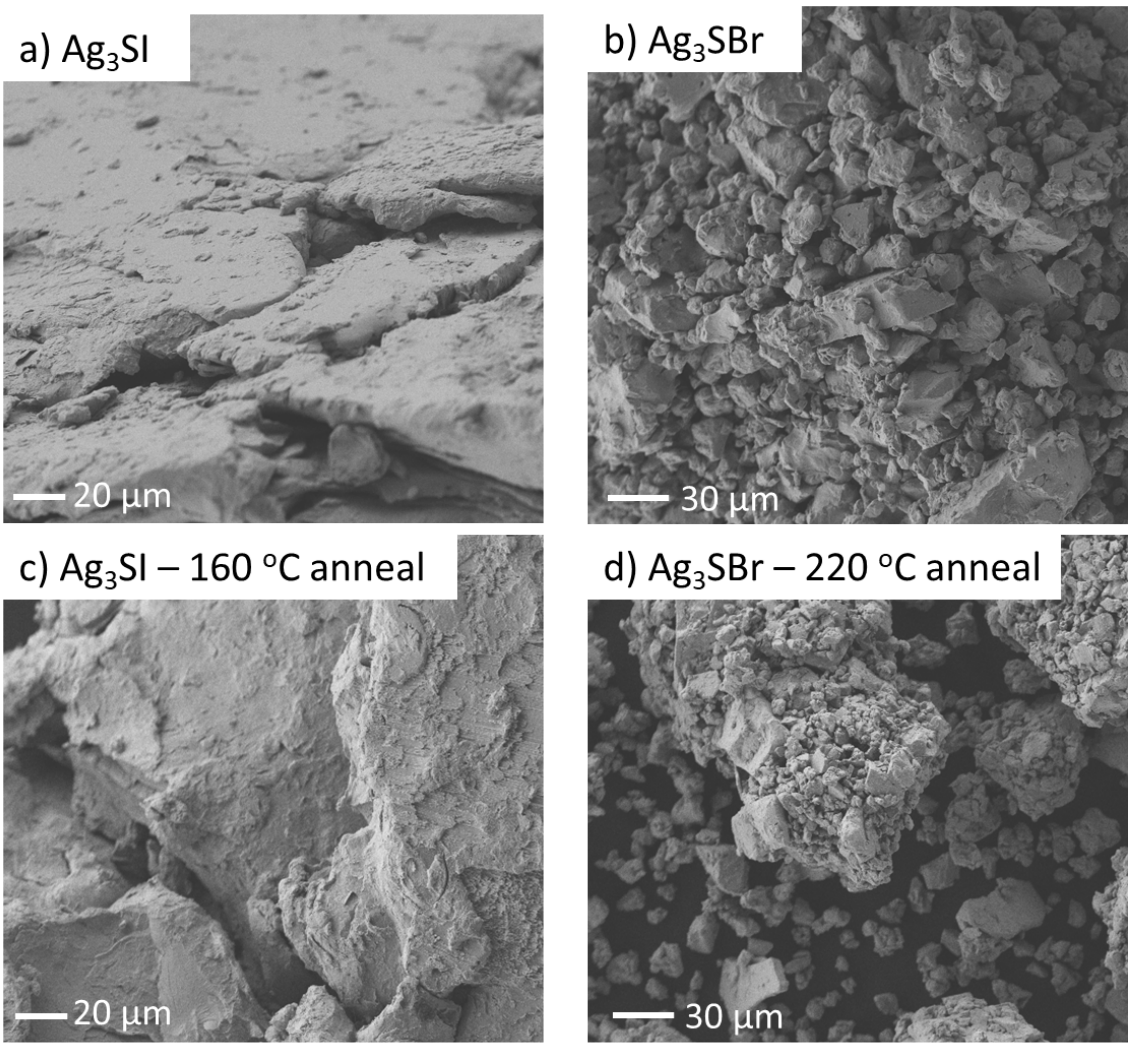

Figure S2. SEM of Ag_3SI (a) and Ag_3SBr (b) powders. Also provided is the annealed Ag_3SI powders; 160 °C for 30 min (c) and the annealed Ag_3SBr powders; 220 °C for 1 hr (d). While the XRD showed the clear formation of antiperovskite phases, there is little observable difference in the powder morphology.

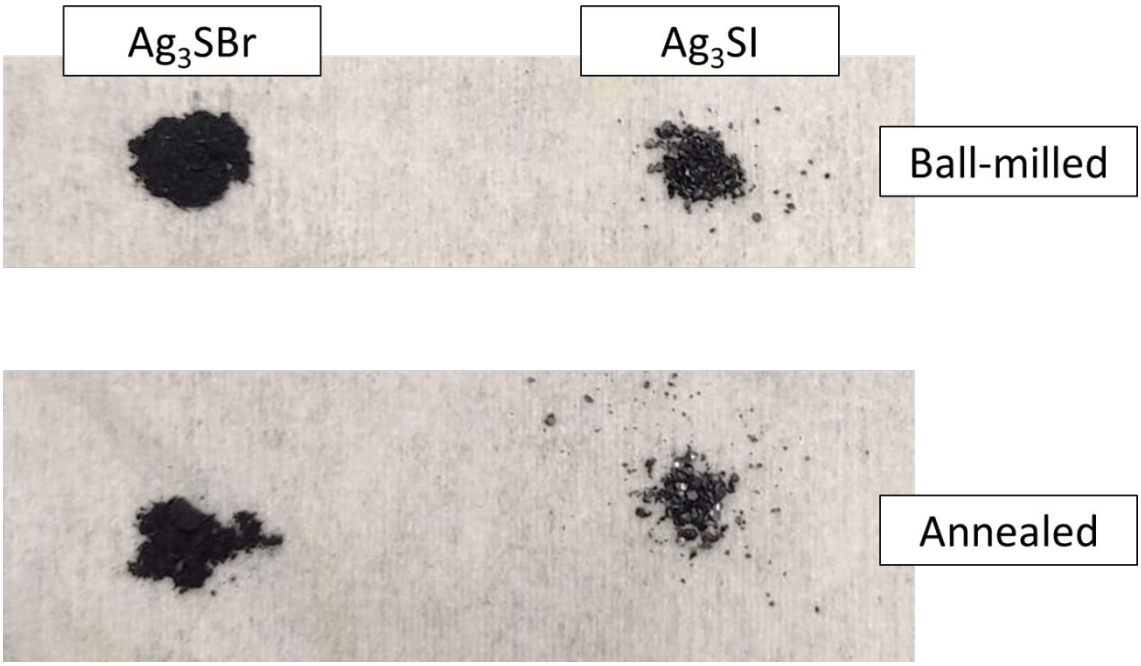

Figure S3. Pictures of the Ag_3SI and Ag_3SBr are included. Both powders are black, but the Ag_3SI has formed with much larger particulate sizes. No apparent difference can be seen between ball-milled and subsequently annealed powders. The Ag_3SI was annealed at 160 ^{o}C for 30 min and the Ag_3SBr at 220 ^{o}C for 1 hr.

Table S1. EDX scans of the SEM images shown in Fig. SX were performed, with the at% Ag, S, and I or Br contents displayed below. The stoichiometric ratios of Ag:S:X (where X is I or Br) is as expected across all compositions (annealed or not annealed), close to 3:1:1.

Material	Ag (at%)	S (at%)	X (I, Br) (at%)
Ag_3SI	53.8	27.07	19.1
Ag_3SI (160 ^oC; 30 min)	61.3	20.1	18.7
Ag_3SBr	64.3	17.9	17.6
Ag_3SBr (220 ^oC; 1 hr)	62.6	19.3	18.0

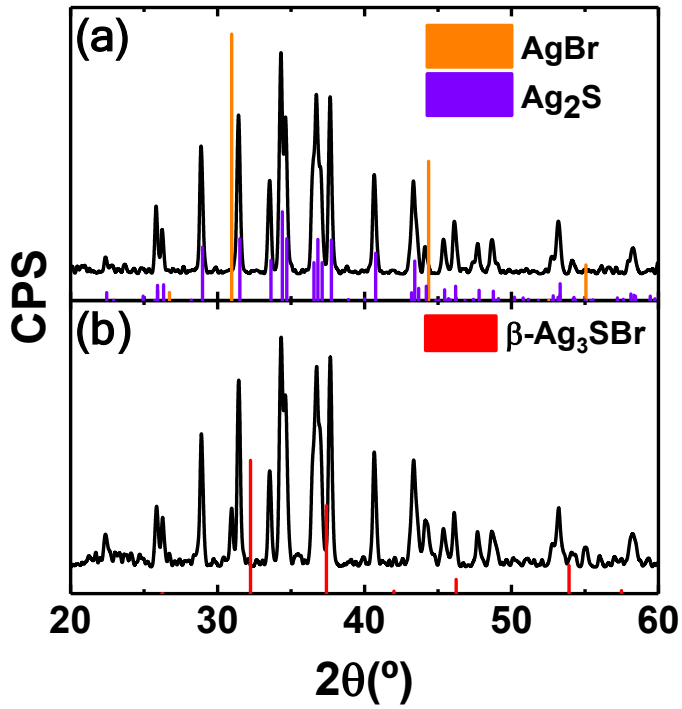

Figure S4. (a) XRD of a hand-mixed stoichiometric AgBr+Ag_2S mixture. Reference patterns for AgBr and Ag_2S correspond to ICSD entries #56546 and #182916, respectively. (b) XRD of the resulting powder after thermal annealing in nitrogen at 160 ºC for 30 min. Reference pattern for β-Ag_3SBr corresponds to ICSD entry #25531.

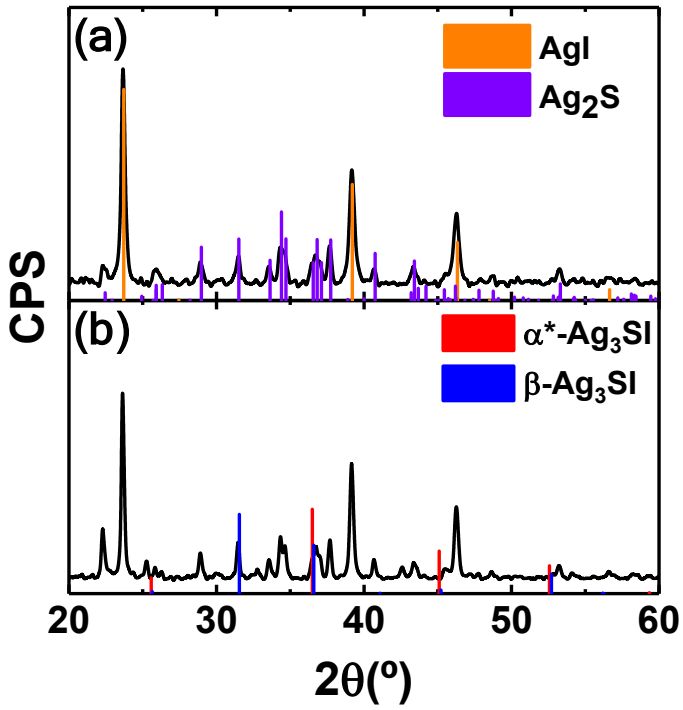

Figure S5. (a) XRD of a hand-mixed stoichiometric AgI+Ag_2S mixture. Reference patterns for AgI and Ag_2S correspond to ICSD entries #56552 and #182916, respectively. (b) XRD of the resulting powder after thermal annealing in nitrogen at 160 ºC for 30 min. Reference patterns for α*-Ag_3SI and β-Ag_3SI correspond to ICSD entries #93429 and #202120, respectively.

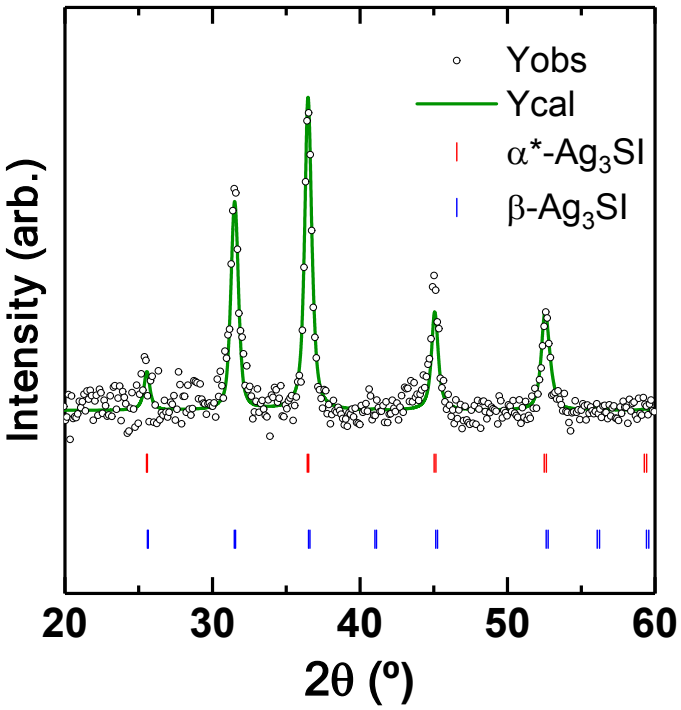

Figure S6. Rietveld refinement of post-ball-milling annealed Ag_3SI powders. The results of these refinements are presented in Table S1. We must note a weak signal around 2θ=28° whose origin is unclear.

Table S2. Phase composition of annealed Ag_3SI powders extracted from Rietveld refinement from Figure S5.

Phase	Composition (%)	Space group	a (Å)	b (Å)	c (Å)	α (°)	β (°)	γ (°)	Rwp (%)	GoF	χ^2
α*-Ag_3SI	75	*Im-3m*	4.92	4.92	4.92	90	90	90	34.8	1.2	1.55
β-Ag_3SI	25	*Pm-3m*	4.91	4.91	4.91	90	90	90			

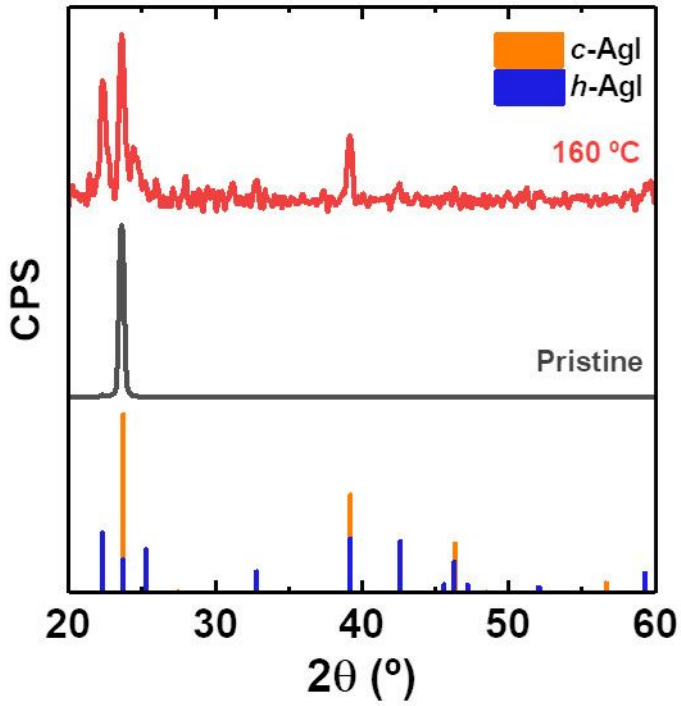

Figure S7. XRD analysis of the pristine and annealed (160 ºC for 30 min) thin films of Ag_3SI prepared by the vacuum single-source evaporation of the ball-milled powder. Reference patterns for cubic AgI (*c*-AgI) and hexagonal AgI (*h*-AgI) are based on ICSD references #56552 and #200104, respectively. Pristine film presents the main peak of cubic AgI but upon annealing it evolves to its hexagonal analogue.

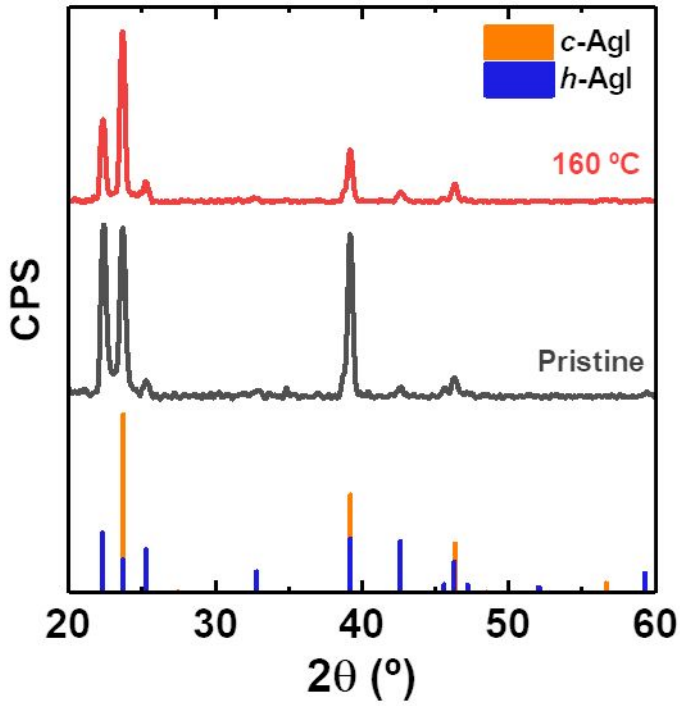

Figure S8. XRD analysis of the pristine and annealed (160 ºC for 30 min) thin films prepared by thermal dual-source (AgI+ Ag_2S) evaporation. Reference patterns for cubic AgI (*c*-AgI) and hexagonal AgI (*h*-AgI) are based on ICSD references #56552 and #200104, respectively. As in the case of single source, pristine film presents the main peak of cubic AgI but upon annealing it evolves to its hexagonal analogue. No evidence of Ag_2S incorporation into the AgI matrix was detected.

Table S3. EDX analysis of thin-films deposited with a laser fluence of 2, 0.75, and 0.3 J/cm^2. These films were deposited using a stoichiometric target of Ag_3SI at a frequency of 10 Hz and working pressure of 1.5×10^{-2} mbar. It can be observed, that by changing the fluence, the Ag:I ratio can be tuned from 3.73 (an iodide deficit) at 2 J/cm^2 to 2.07 (an iodide excess) at 0.75 J/cm^2.

Atomic Ratios				
Fluence	**Ag (at %)**	**S (at %)**	**I (at %)**	**Ag:I ratio**
2 J/cm^2	71.6	9.2	19.2	3.73
0.75 J/cm^2	61.2	9.2	29.6	2.07
0.3 J/cm^2	58.4	5.8	35.8	1.63

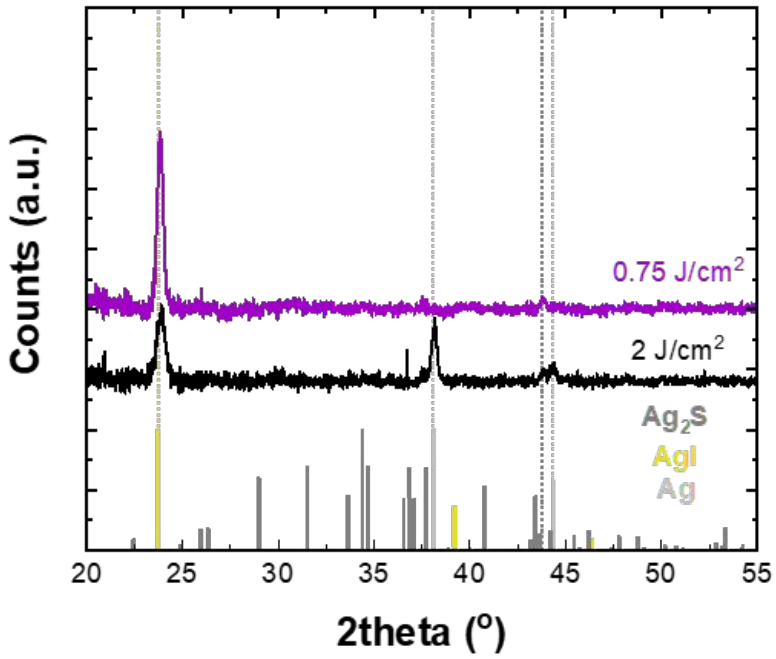

Figure S9. XRD of thin-films deposited using a stoichiometric target of Ag_3SI, varying the fluence from 2 J/cm^2 (black) to 0.75 J/cm^2 (purple). From the EDX results reported in Table S4, it can be seen that the sample deposited at 0.75 J/cm^2 is Ag-poor, and the as deposited film shows a strong AgI peak, with a faint peak at 43.77^0 attributed to Ag_2S. Meanwhile, the 2 J/cm^2 sample, shown to be Ag-rich in Table S4, shows the nucleation of a metallic Ag phase. Since metallic silver can be harmful to devices, we choose to pursue the 0.75 J/cm^2 process.

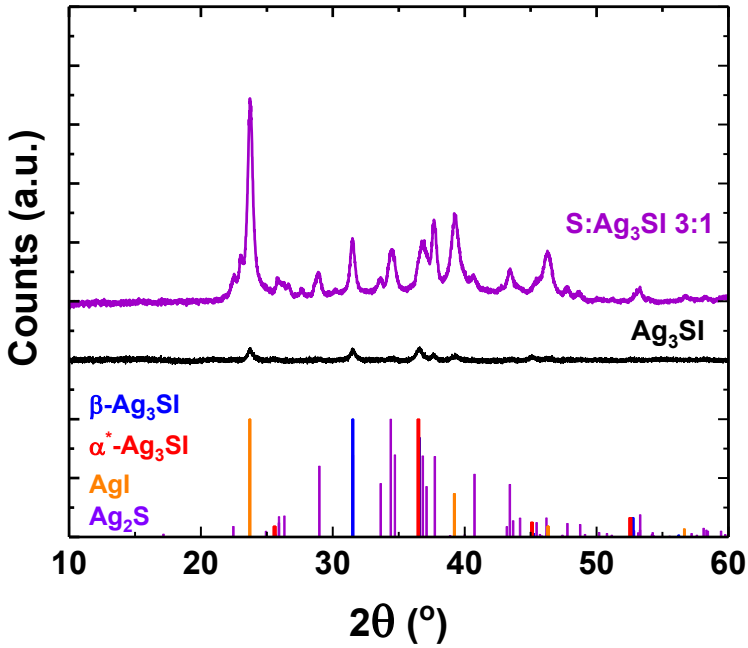

Figure S10. XRD of pressed Ag_3SI targets show that the phase-purity seen in the powders is not retained during the target fabrication. The stoichiometric target (shown in black) has prominent AgI peaks. Target with sulphur excess 3:1 shows additional phases related to Ag_2S, AgI, and Ag_3SI polymorphs.

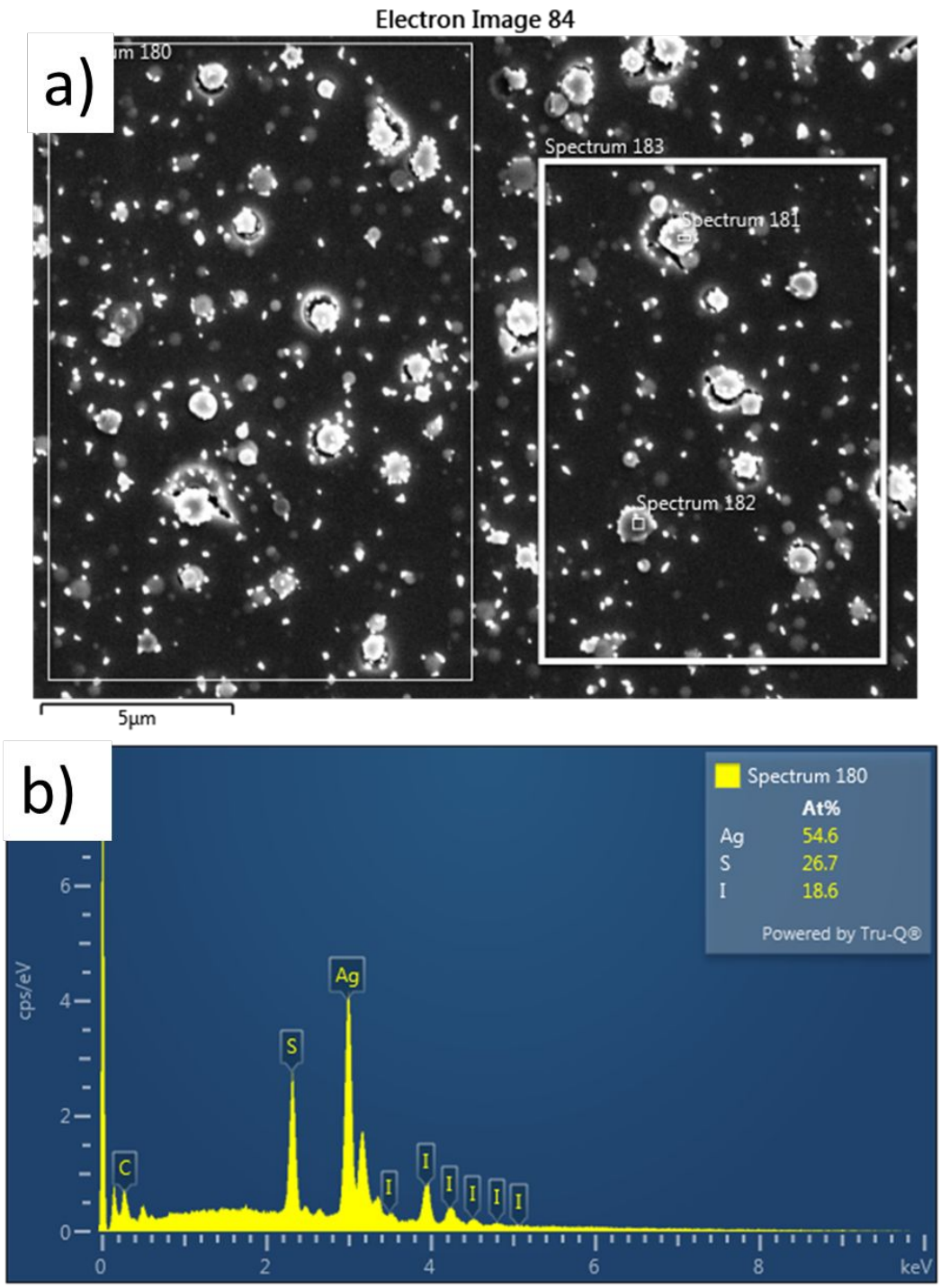

Figure S11. SEM (a) and EDX (b) of pristine Ag_3SI thin-film. A sulphur excess is noted, with many additional peaks seen in the EDX spectrum and prescribed to the substrate (fused silica/ITO/SnO_x).

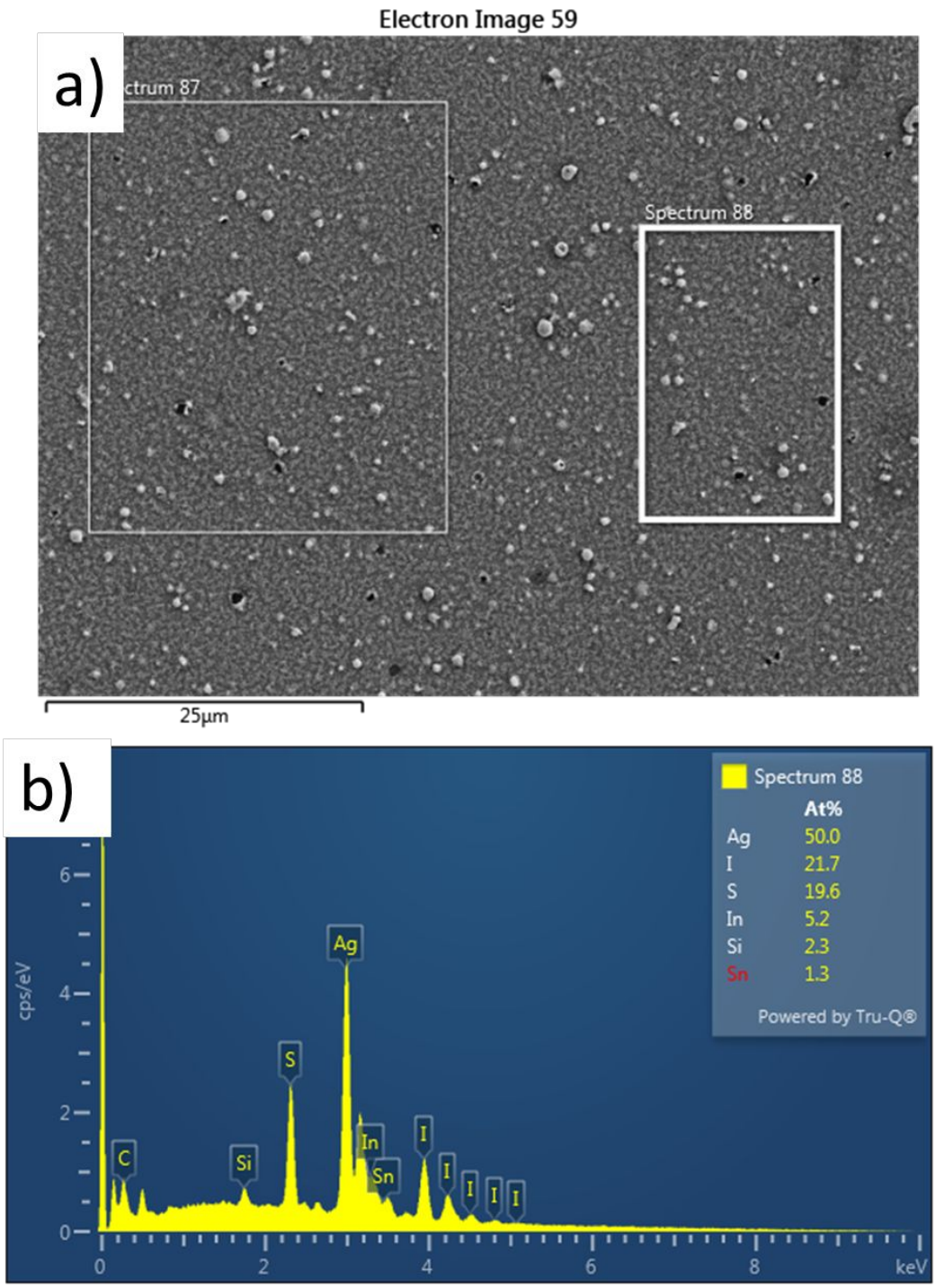

Figure S12. SEM (a) and EDX (b) of annealed Ag_3SI thin-film. Here, the ratios of Ag:S:I have equalized, attributed to sulfur leaving the film. Many extra peaks are shown, prescribed to the substrate used (fused silica, ITO, SnO_x).

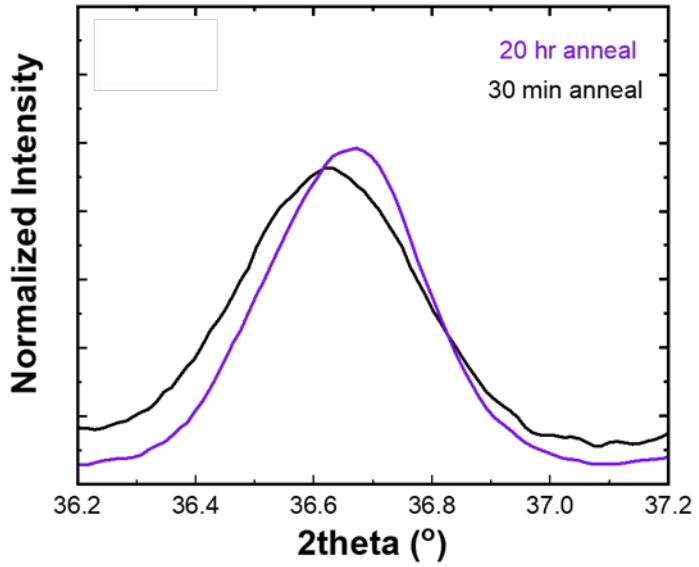

Figure S13. Zoom-in section of the XRD peak at 36.6º of thin-films deposited using a sulphur-rich target of 3:1 S:Ag_3SI (Figure 6).

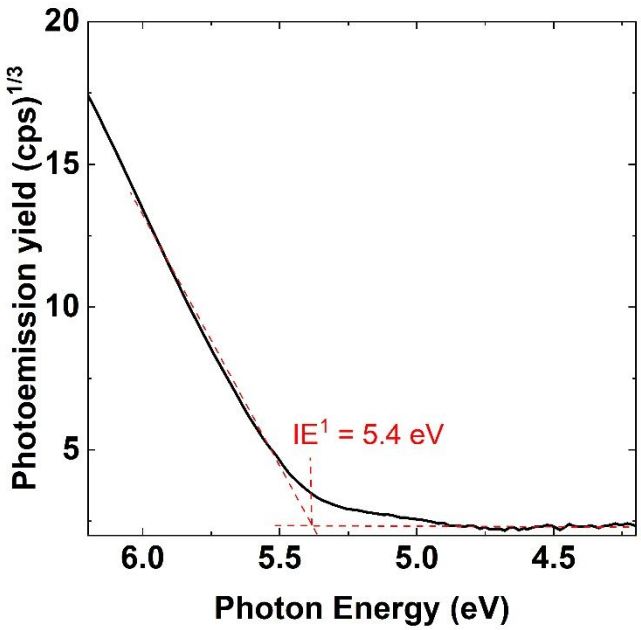

Figure S14. Air photoelectron spectroscopy characterization of Ag3SI thin film. Linear extrapolation of the onset suggests a ionization energy around 5.4 eV. See Figure 4d and its discussion in the main text for more details.

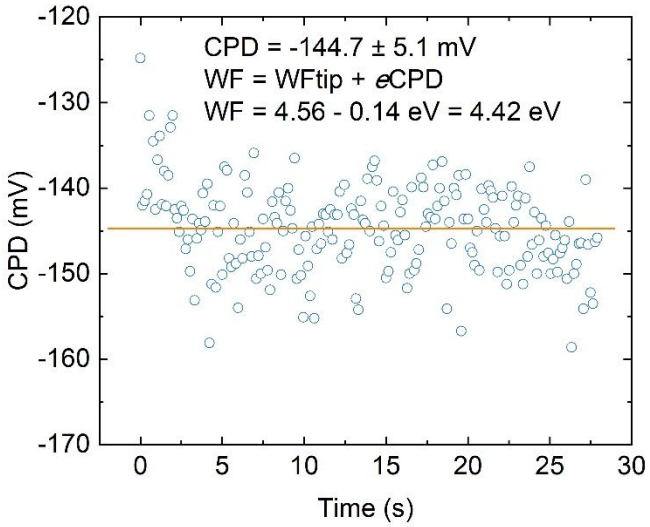

Figure S15. Kelvin probe characterization of Ag3SI thin film yielding a work function of 4.4 eV.

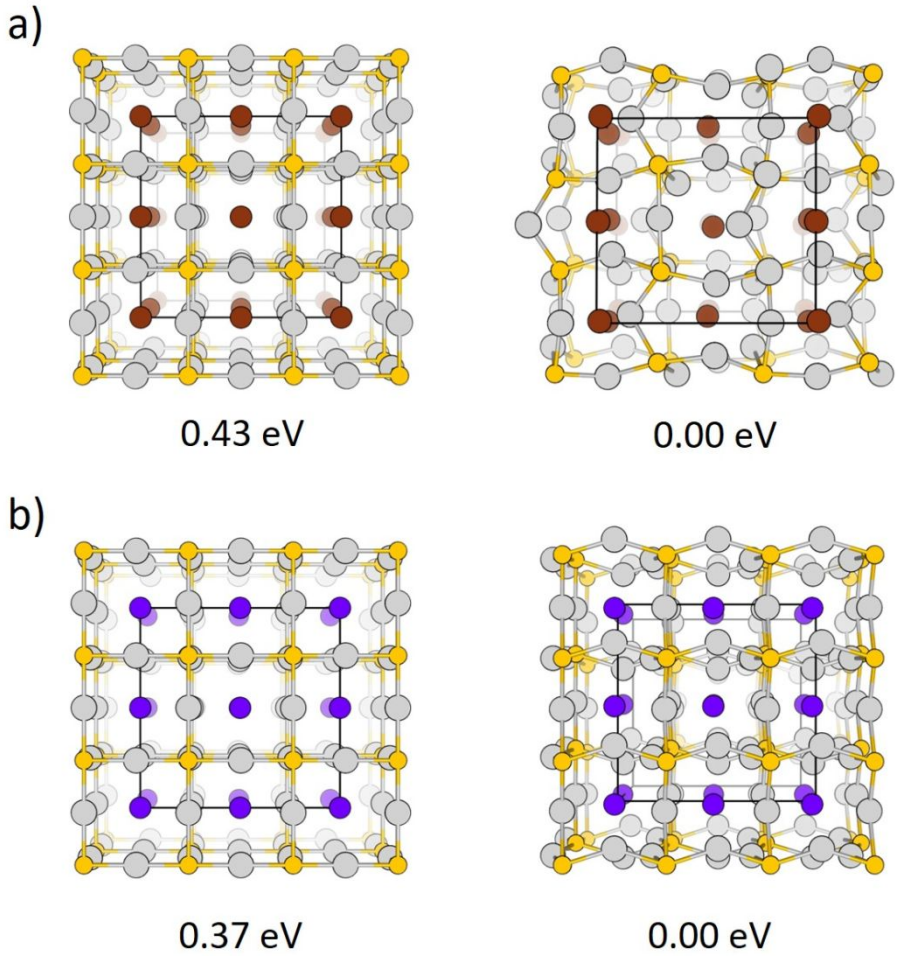

Figure S16. Optimized crystal structures calculated at the PBEsol/tier-1 level for the face-centered transition state (left) and the minimum-energy β-distorted phase (right) of a 2×2×2 extended β-$Pm\bar{3}m$ cell of Ag_3SBr (a) and Ag_3SI (b). The relative energy per Ag_3SX unit computed for the two polymorphs is indicated. Color coding: gray for Ag, yellow for S, maroon for Br, and purple for I.

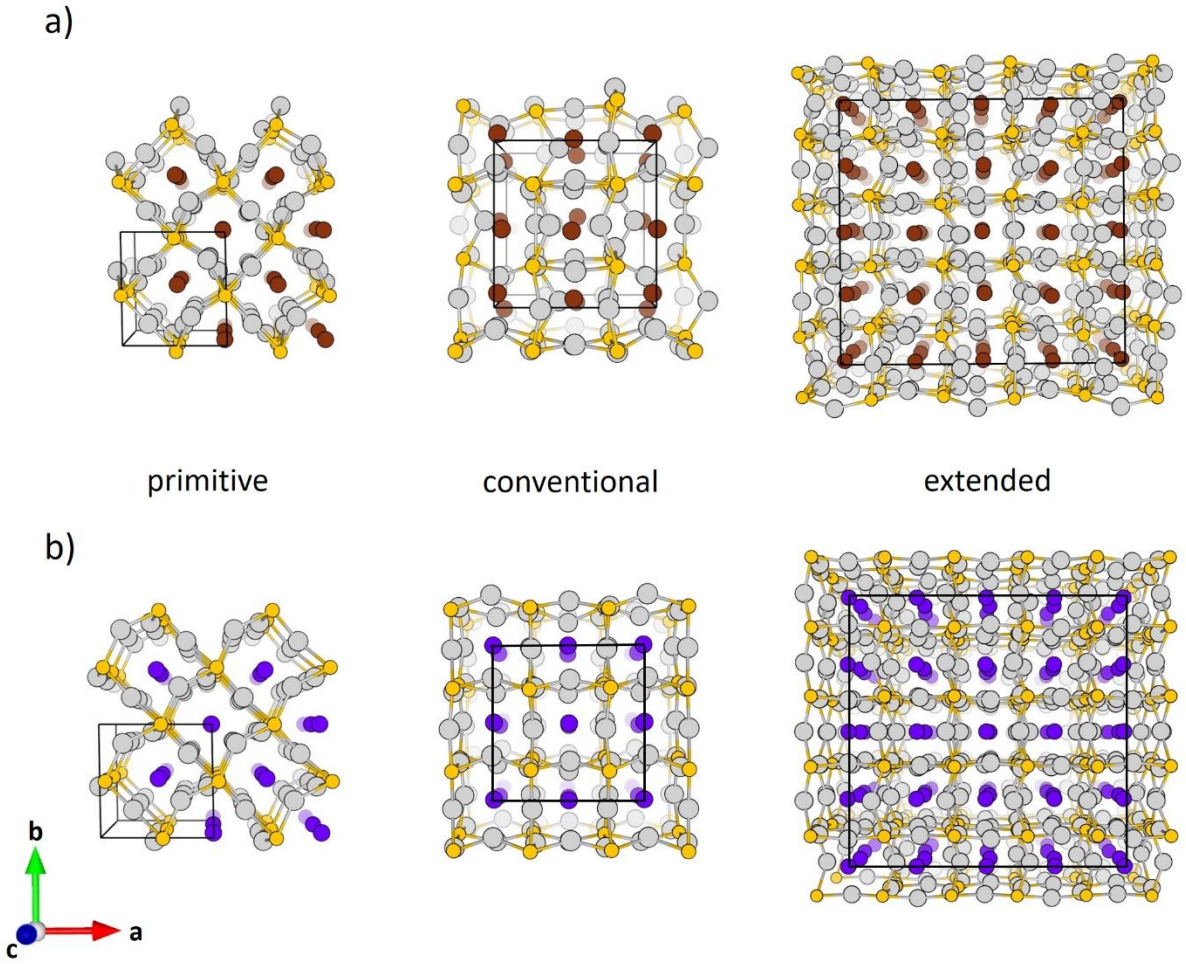

Figure S17. Minimum-energy crystal structures computed at the PBEsol/tier-1 level for different "β"-ordered $Cmcm$ cells (primitive, conventional, and 2×2×2 conventional extended) of Ag_3SBr (a) and Ag_3SI (b). Color coding: gray for Ag, yellow for S, maroon for Br, and purple for I.

Table S4. Lattice parameters (lengths in Å and angles in deg) computed at the PBEsol/tier-1 level for the minimum-energy crystal structures of different cells of Ag_3SBr and Ag_3SI. ORCC, ORC, RHL, and HEX refer to C-centered orthorhombic, orthorhombic, rhombohedral, and hexagonal Bravais lattice, respectively.

System	Cell (Bravais lattice)		a	b	c	α	β	γ
Ag_3SBr ($Cmcm$)	primitive	(ORCC)	8.9594	6.5476	7.1195	90	90	90
	conventional	(ORC)	9.1310	9.3873	9.9030	90	90	90
	extended	(ORC)	18.1748	18.8074	19.5264	90	90	90
Ag_3SI ($Cmcm$)	primitive	(ORCC)	9.6539	6.8098	6.8465	90	90	90
	conventional	(ORC)	9.2265	9.5030	10.1460	90	90	90
	extended	(ORC)	18.5186	18.9979	20.2204	90	90	90
Ag_3SI ($R3$)	primitive	(RHL)	4.8292	-	-	89.91	-	-
	conventional	(HEX)	6.8420	-	8.3189	-	-	120
	extended	(HEX)	13.6744	-	16.6820	-	-	120

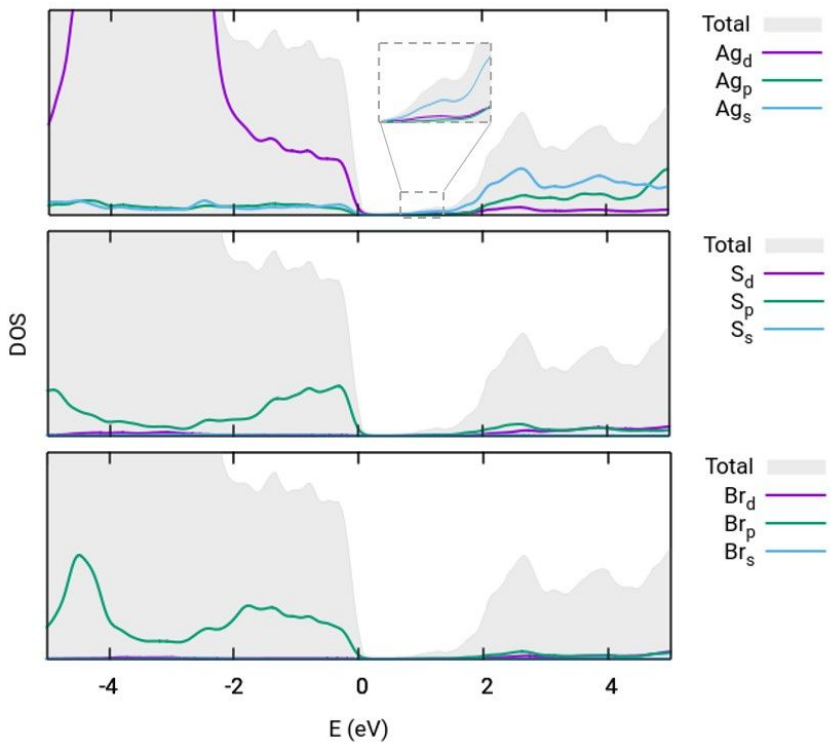

Figure S18. Mulliken orbital-projected density of states calculated at the PBEsol level for the primitive ORCC cell of Ag_3SBr.

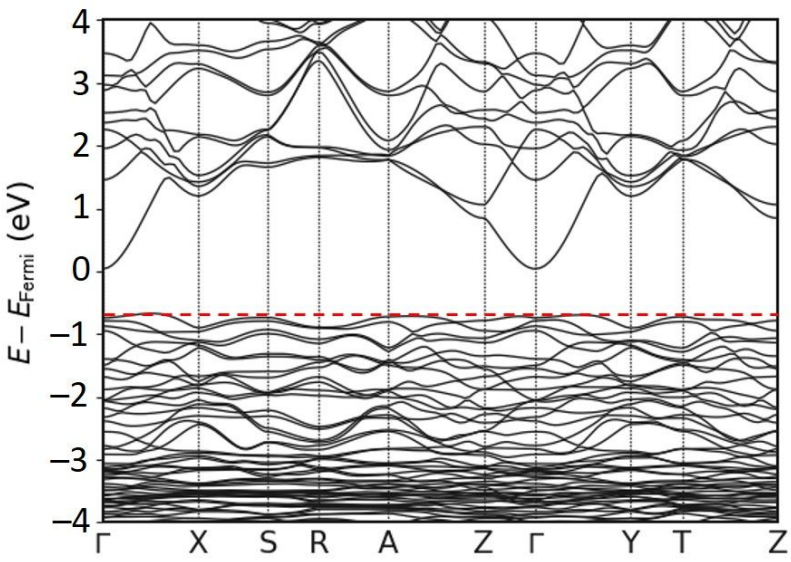

Figure S19. Band structure calculated at the PBEsol level for the primitive ORCC cell of Ag_3SBr. An indirect (T→Γ)/direct (Γ) bandgap of 0.56/0.78 eV is obtained.

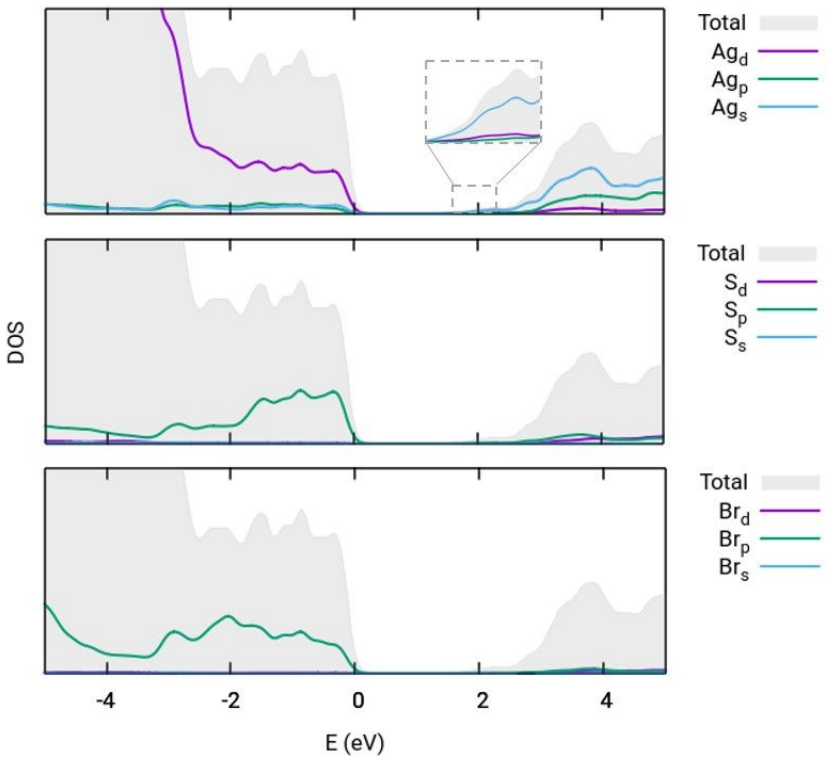

Figure S20. Mulliken orbital-projected density of states calculated at the HSE06+SOC level for the primitive ORCC cell of Ag_3SBr.

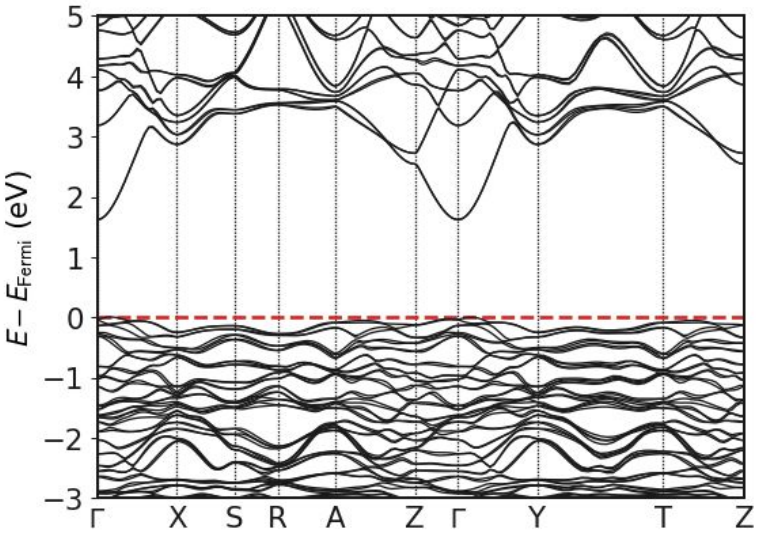

Figure S21. Band structure calculated at the HSE06+SOC level for the primitive ORCC cell of Ag_3SBr.

Table S5. Bandgap energies (in eV) calculated at different levels of theory for different crystal systems and cells of Ag_3SBr and Ag_3SI.

		Bandgap (indirect/direct)			
System	**Cell**	**PBEsol**	**PBEsol+SOC**	**HSE06**	**HSE06+SOC**
Ag_3SBr ($Cmcm$)	primitive	0.556/0.782	0.544/0.770	1.502/1.695	1.487/1.660
	conventional	0.490/0.674	0.479/0.647	1.431/1.609	1.417/1.579
	extended	0.514	-	-	1.436
Ag_3SI ($Cmcm$)	primitive	0.492/0.697	0.335/0.604	1.437/1.649	1.276/1.557
	conventional	0.119/0.276	0.084/0.207	1.018/1.163	0.824/1.064
	extended	0.294	-	-	0.995
Ag_3SI ($R3$)	primitive	0.545/0.878	0.385/0.764	1.498/1.879	1.336/1.712
	conventional	0.521/0.880	0.356/0.768	1.480/1.846	1.316/1.686
	extended	0.615	-	-	1.416

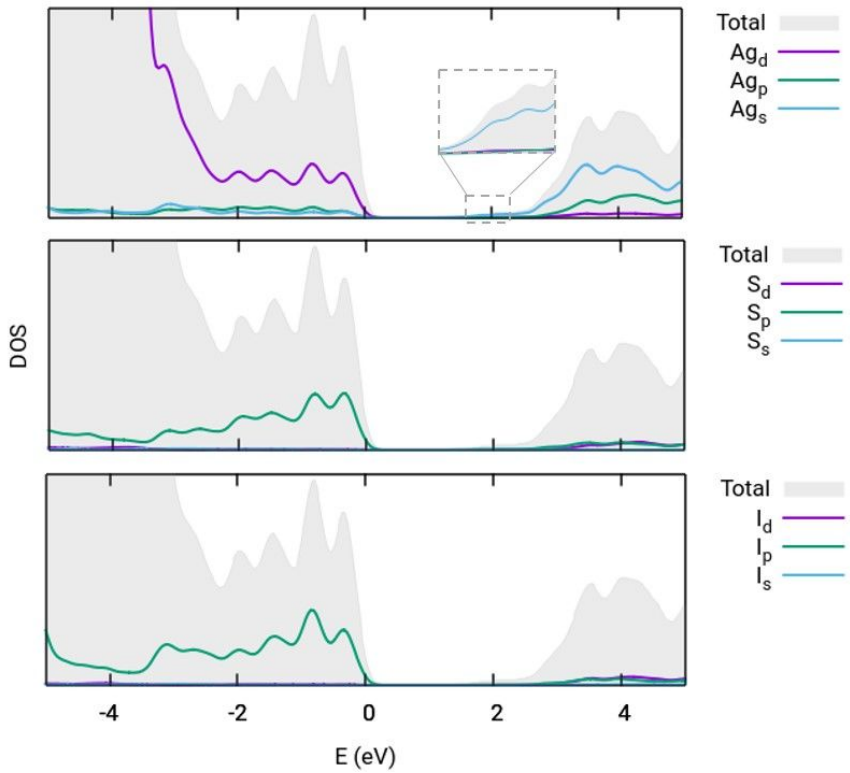

Figure S22. Mulliken orbital-projected density of states calculated at the HSE06+SOC level for the primitive ORCC cell of Ag_3SI.

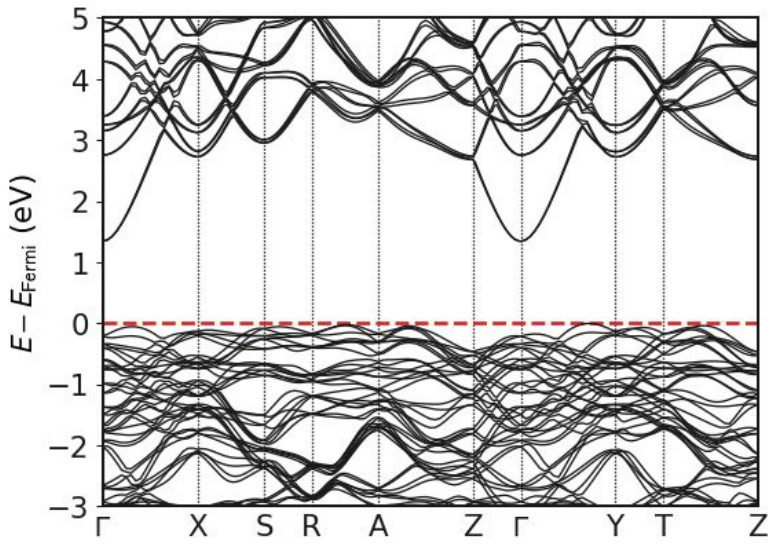

Figure S23. Band structure calculated at the HSE06+SOC level for the primitive ORCC cell of Ag_3SI.

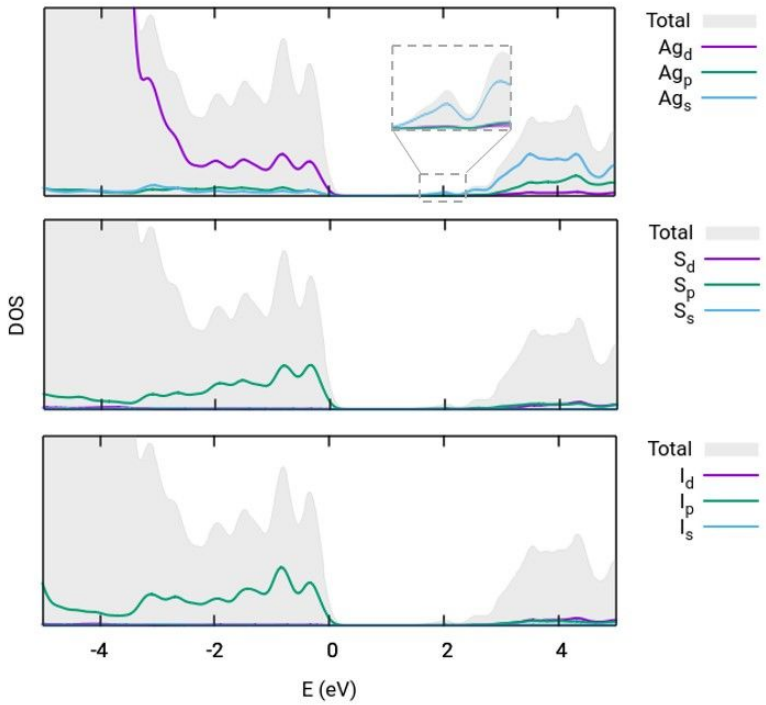

Figure S24. Mulliken orbital-projected density of states calculated at the HSE06+SOC level for the conventional HEX cell of Ag_3SI.

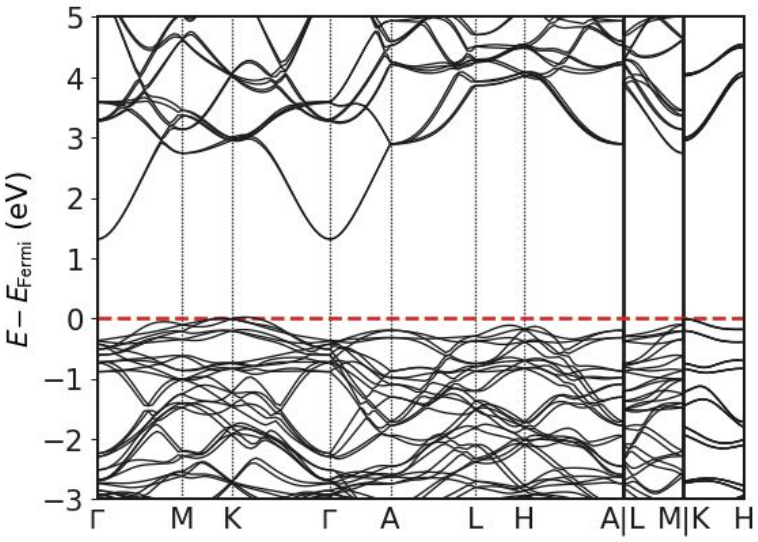

Figure S25. Band structure calculated at the HSE06+SOC level for the conventional HEX cell of Ag_3SI.

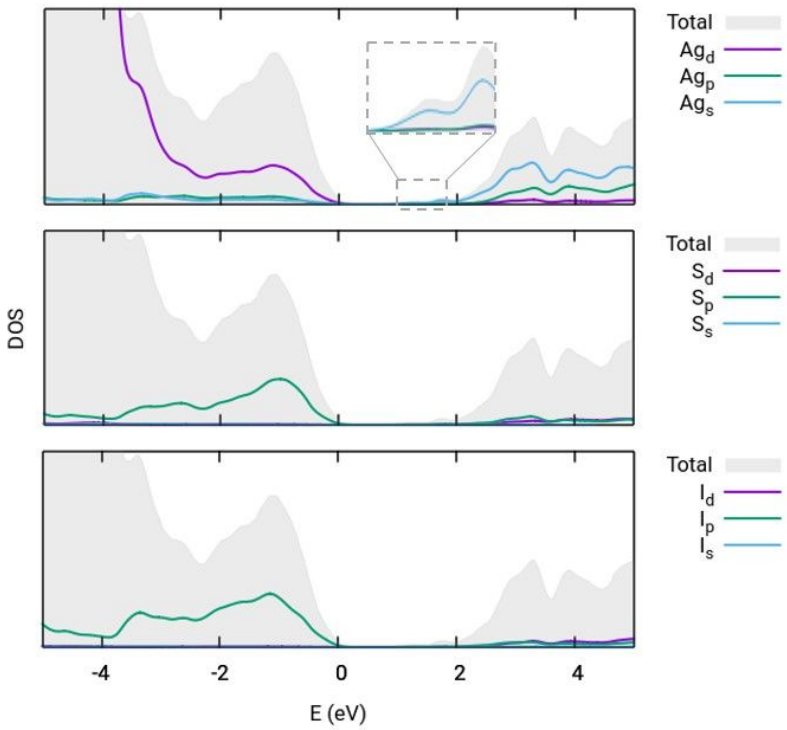

Figure S26. Mulliken orbital-projected density of states calculated at the HSE06+SOC level for the conventional ORC cell of Ag_3SI.

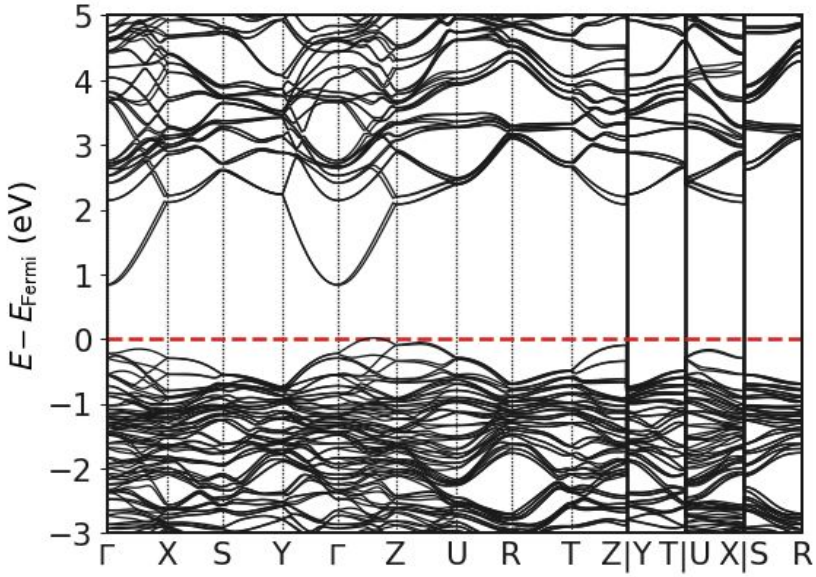

Figure S27. Band structure calculated at the HSE06+SOC level for the conventional ORC cell of Ag_3SI.

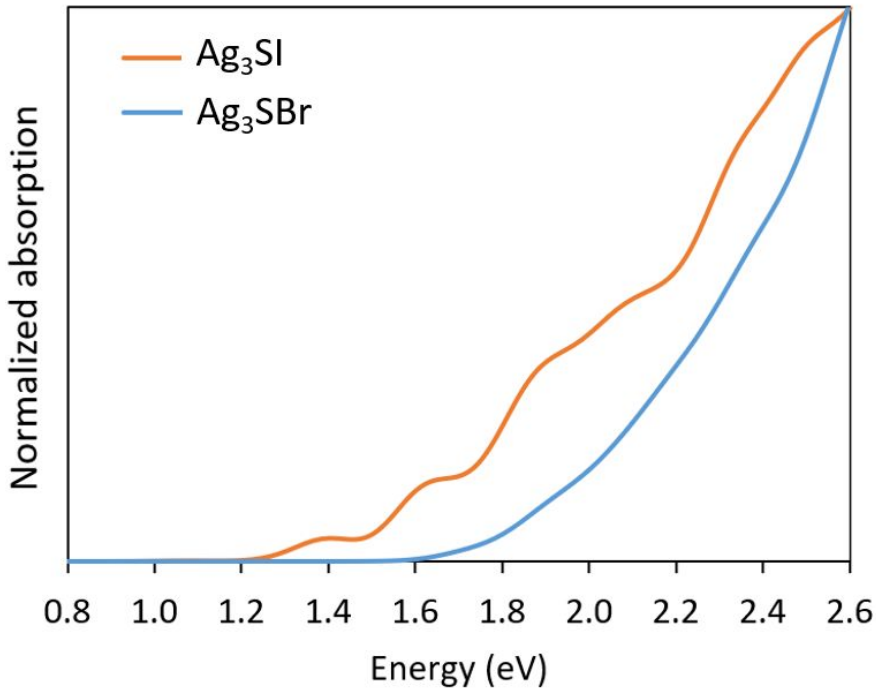

Figure S28. Simulated absorption spectrum calculated for Ag_3SX at the HSE06+SOC level using the linear macroscopic dielectric function approximation.

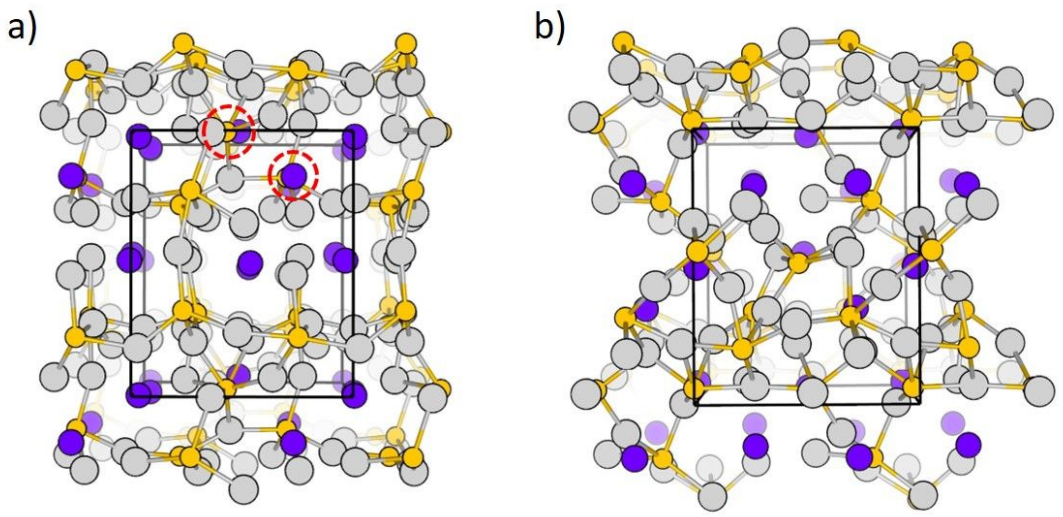

Figure S29. Minimum-energy crystal structures calculated at the PBEsol level for the conventional unit cell of α*-Ag_3SI with 15% (a) and 100% (b) S^{2-}/I^- random distributions. The exchanged S^{2-}/I^- pair in a) is highlighted. Color coding: gray for Ag, yellow for S, and purple for I.

Table S6. Root-mean-square deviation (RMSD) in the atomic positions along the ab-initio molecular dynamics with respect to the initial (static) crystal structure.

Atom type	RMSD Average (Å)	Standard deviation (Å)
Ag_3SI		
All	0.779	0.297
Ag	0.845	0.361
S	0.794	0.304
I	0.447	0.127
Ag_3SBr		
All	0.973	0.300
Ag	1.111	0.375
S	0.744	0.191
Br	0.662	0.185

REFERENCES:

(1) Jackson, W. B.; Amer, N. M.; Boccara, A. C.; Fournier, D. Photothermal Deflection Spectroscopy and Detection. *Appl. Opt.* **1981**, *20* (8), 1333–1344.

(2) Blum, V.; Gehrke, R.; Hanke, F.; Havu, P.; Havu, V.; Ren, X.; Reuter, K.; Scheffler, M. Ab Initio Molecular Simulations with Numeric Atom-Centered Orbitals. *Comput. Phys. Commun.* **2009**, *180* (11), 2175–2196.

(3) Jain, A.; Ong, S. P.; Hautier, G.; Chen, W.; Richards, W. D.; Dacek, S.; Cholia, S.; Gunter, D.; Skinner, D.; Ceder, G.; et al. The Materials Project: A Materials Genome Approach to Accelerating Materials Innovation. *APL Mater.* **2013**, *1* (1), 011002.

(4) Perdew, J. P.; Ruzsinszky, A.; Csonka, G. I.; Vydrov, O. A.; Scuseria, G. E.; Constantin, L. A.; Zhou, X.; Burke, K. Restoring the Density-Gradient Expansion for Exchange in Solids and Surfaces. *Phys. Rev. Lett.* **2008**, *100* (13), 136406.

(5) Heyd, J.; Scuseria, G. E.; Ernzerhof, M. Hybrid Functionals Based on a Screened Coulomb Potential. *J. Chem. Phys.* **2003**, *118* (18), 8207.

(6) Huhn, W. P.; Blum, V. One-Hundred-Three Compound Band-Structure Benchmark of Post-Self-Consistent Spin-Orbit Coupling Treatments in Density Functional Theory. *Phys. Rev. Mater.* **2017**, *1* (3), 033803.

(7) Giannozzi, P.; Baroni, S.; Bonini, N.; Calandra, M.; Car, R.; Cavazzoni, C.; Ceresoli, D.; Chiarotti, G. L.; Cococcioni, M.; Dabo, I.; et al. QUANTUM ESPRESSO: A Modular and Open-Source Software Project for Quantum Simulations of Materials. *J. Phys. Condens. Matter* **2009**, *21* (39).

(8) Giannozzi, P.; Andreussi, O.; Brumme, T.; Bunau, O.; Buongiorno Nardelli, M.; Calandra, M.; Car, R.; Cavazzoni, C.; Ceresoli, D.; Cococcioni, M.; et al. Advanced Capabilities for Materials Modelling with Quantum ESPRESSO. *J. Phys. Condens. Matter* **2017**, *29* (46).

(9) Rodkey, N.; Kaal, S.; Sebastia-Luna, P.; Birkhölzer, Y. A.; Ledinsky, M.; Palazon, F.; Bolink, H. J.; Morales-Masis, M. Pulsed Laser Deposition of Cs2AgBiBr6: From Mechanochemically Synthesized Powders to Dry, Single-Step Deposition. *Chem.*

Mater. **2021**, *33* (18), 7417–7422.

(10) Ulatowski, A. M.; Herz, L. M.; Johnston, M. B. Terahertz Conductivity Analysis for Highly Doped Thin-Film Semiconductors. *J. Infrared, Millimeter, Terahertz Waves* **2020**, *41* (12), 1431–1449.

(11) Xia, C. Q.; Peng, J.; Poncé, S.; Patel, J. B.; Wright, A. D.; Crothers, T. W.; Uller Rothmann, M.; Borchert, J.; Milot, R. L.; Kraus, H.; et al. Limits to Electrical Mobility in Lead-Halide Perovskite Semiconductors. *J. Phys. Chem. Lett.* **2021**, *12* (14), 3607–3617.